

A polyamide-facilitated soldering approach for Mini LED precise alignment leveraging 3D interfacial networks

Ji, Liangzheng; Zhang, Jing; Zhang, Guoqi; Liu, Pan

DOI

[10.1016/j.jsamd.2024.100817](https://doi.org/10.1016/j.jsamd.2024.100817)

Publication date

2024

Document Version

Final published version

Published in

Journal of Science: Advanced Materials and Devices

Citation (APA)

Ji, L., Zhang, J., Zhang, G., & Liu, P. (2024). A polyamide-facilitated soldering approach for Mini LED precise alignment leveraging 3D interfacial networks. *Journal of Science: Advanced Materials and Devices*, 9(4), Article 100817. <https://doi.org/10.1016/j.jsamd.2024.100817>

Important note

To cite this publication, please use the final published version (if applicable). Please check the document version above.

Copyright

Other than for strictly personal use, it is not permitted to download, forward or distribute the text or part of it, without the consent of the author(s) and/or copyright holder(s), unless the work is under an open content license such as Creative Commons.

Takedown policy

Please contact us and provide details if you believe this document breaches copyrights. We will remove access to the work immediately and investigate your claim.



Research Article

A polyamide-facilitated soldering approach for Mini LED precise alignment leveraging 3D interfacial networks

Liangzheng Ji^{a,b}, Jing Zhang^b, Guoqi Zhang^c, Pan Liu^{a,*}

^a Academy for Engineering and Technology, Fudan University, Shanghai, 200433, China

^b Heraeus Materials Technology Shanghai Ltd., Shanghai, 201100, China

^c Electronic Components, Technology, and Materials, Delft University of Technology, Delft, 2628CD, Netherlands

ARTICLE INFO

Keywords:

Mini LED
Precise alignment
Soldering
3D interfacial networks

ABSTRACT

Driven by the need for improved quality, energy efficiency, and visual innovation, display technology has evolved from CRT to Mini LED. However, the transfer process in Mini LED assembly poses challenges in precision. This study addressed the displacement issue during the transfer process by investigating the synergistic effects of solder and functional organic chemicals. Through the Mini LED assembly process, with the Mini LED size measuring 150 μm (length) * 100 μm (width) * 70 μm (thickness), polyamide was identified as a facilitator for precise alignment, which enhanced self-alignment capabilities by 68.8 % and improved the accuracy on self-aligned distance from 12.5 μm to 21.1 μm in Mini LED packaging. Through the powder coalescence approach, further extensive analysis using XPS, SEM, FTIR, and DSC reveals the synergistic effects. It supports the proposed three-dimensional polyamide-tin ion coordination interfacial network construction mechanism that facilitates solder-to-solder self-alignment and coalescence. This study provides insight into such a polymer-metal ion 3D coordination network for Mini LED precise alignment, which is promising for mass production.

1. Introduction

The evolution of display technology has undergone transitions from cathode ray tubes (CRT) to liquid crystal displays (LCD) and eventually to organic light-emitting diodes (OLED), Mini LEDs, and Micro LEDs [1–10]. The need for improved display quality, energy efficiency, and innovation in visual technologies has driven this progression. The emergence of Mini LED technologies has pushed the boundaries of display innovation for higher resolutions and better color reproduction [3,4,9]. Mini LED displays represent the next evolution in backlighting technology. They utilize a large number of miniaturized LED backlights to provide precise local dimming and improved contrast ratios compared to traditional LCDs. Besides, Mini LED technology has gained traction in high-end displays, where it offers enhanced HDR performance and better energy efficiency. Micro LED displays take the evolution even further by integrating even smaller LED elements, leading to higher pixel densities, enhanced brightness levels, and improved energy efficiency. Therefore, Mini LED technology has the potential to deliver ultra-high resolution, high dynamic range, and a wide color gamut, making it a promising candidate for future display innovations [2,9,10].

In both Mini LED backlighting and display technologies, the picking and placing process is necessary for Mini LED transfer. The continual decrease in Mini LED size presents substantial challenges for the assembly process of Mini LED technology. The inherent trade-off between transfer speed and precision becomes increasingly pronounced, high-speed transfer often results in reduced accuracy, whereas high-precision transfer tends to comprise transfer efficiency. This issue has led to challenges in terms of precision, yield rates, and overall manufacturing costs, although ongoing research and development efforts aim to address these challenges brought forth by the relentless miniaturization of LEDs and unlock the potential of smaller LED technology, especially [1,11–21].

Besides transfer, soldering technology also helps with high precision, with the capability of self-alignment. Tin-based soldering techniques are commonly employed due to their excellent electrical and thermal conductivity, mechanical properties, and compatibility with the materials used in electronic packaging including processes related to the Mini LED packaging [22–28]. Tin's self-alignment capability refers to its ability to undergo a self-correcting process during reflow soldering, aligning itself with the intended mating surfaces to form strong and reliable solder

Peer review under responsibility of Vietnam National University, Hanoi.

* Corresponding author. Academy for Engineering & Technology, Fudan University, Shanghai 200433, China.

E-mail address: panliu@fudan.edu.cn (P. Liu).

<https://doi.org/10.1016/j.jسامd.2024.100817>

Received 10 September 2024; Received in revised form 13 November 2024; Accepted 17 November 2024

Available online 19 November 2024

2468-2179/© 2024 Vietnam National University, Hanoi. Published by Elsevier B.V. This is an open access article under the CC BY-NC-ND license (<http://creativecommons.org/licenses/by-nc-nd/4.0/>).

joints. In the electronics industry, tin's self-alignment capability is leveraged during the soldering of surface mount components on targeted substrate and the assembly of semiconductor devices [29]. During the reflow soldering process, molten tin automatically aligns itself with the contact pads of electronic components and the corresponding pads on the PCB, ensuring precise and accurate solder joint formation. The self-aligning nature of tin contributes to the precise positioning and bonding of miniaturized components, enabling the manufacturing of intricate microsystems and devices with high levels of accuracy and repeatability [18,30–34]. For Mini LED, tin's capability for self-correcting during reflow soldering aligns with the specific placement requirements, offering a potential solution to the precise alignment and bonding challenges inherent in Mini LED assembly. By leveraging tin's self-alignment properties, manufacturers could potentially mitigate misalignment issues, enhance chip placement accuracy, and improve the overall reliability of Mini LED displays. So far, for tin-based soldering technology in general, the role of organic chemicals in precise alignment has become paramount [35].

To our knowledge, limited studies were focused on investigating the effects of functional polymers on self-alignment properties. Polyamide, a prototypical thixotropic agent, has been extensively utilized in the realm of solder paste applications to significantly enhance anti-sagging performance [36]. In the course of our research, we have discovered that polyamide substantially enhance the self-alignment capabilities of tin during the soldering process. Polyamide, characterized by their distinctive amide groups, stand out as exceptional hydrogen bond donors and acceptors, offering crucial active sites in Fig. 1 (a). Moreover, during the reflow process, these groups function as potent ligands, coordinating with metals or metal ions (Fig. 1 (b)) to establish polymeric networks that enhance interparticle affinity. When polyamide was applied to the packaging of the Mini LED, enhanced self-alignment with improved accuracy was achieved, as shown in Fig. 2 (a) and its corresponding schematic in Fig. 2 (b). The soldering interface in this case is between tin and tin, which essentially relates to the fusion between tin balls, as shown in Fig. 2 (d). In practical terms, this corresponds to an experiment where a mass of solder powder is coalesced into a tin ball, as illustrated in Fig. 2 (c). Due to the potential interference of other substances in the flux, we have designed the experiment with tin balls to simplify the formulation composition. Moreover, we utilize the process described in Fig. 2 (f) that involves formic acid-assisted vacuum reflow. This formic acid-assisted soldering process offers a more intuitive means to observe and analyze the influence of the organic compound, especially in comparison to the conventional reflow process, as depicted in Fig. 2 (e). In the solder ball coalescence experiment, the strong coalescence ability of polyamide was observed, capable of pulling the solder powder together to form a solder ball under different conditions, as depicted in Fig. 2 (d). A comprehensive analysis of the intricate interactions between organic materials and metals in the domain of soldering was then conducted using XPS, SEM, FTIR, and DSC characterization techniques. These characterization techniques supported the proposed mechanism of constructing a three-dimensional polyamide-tin ion coordination interfacial network that facilitates solder-to-solder self-alignment and coalescence. This investigation

contributes to an enriched understanding and provides a distinct point for precise self-assembly. Moreover, a robust theoretical framework was established through this investigation to underpin the exploration of interactions between metal particles and organic substances.

2. Experimental

2.1. Preparation of modified flux and activator-free solder paste

In this study, we prepared a modified flux to investigate the self-alignment properties of polyamide. The modified flux comprised 95 % base flux and 5 % polyamide by mass ratio, the base flux, known as LED140 Flux-P, while the polyamide, known as R-PA-1, were both obtained from the Heraeus group. The two components were blended at an elevated temperature of 130 °C for 20 min to ensure homogenous blending and minimize solvent evaporation, thus maintaining the flux in a liquid state.

In the solder ball coalescence experiment, the activator-free solder paste was designed to primarily stimulate self-alignment performance and study the fundamental mechanism of self-alignment. The manufacturing process involved two steps. First, various fluxes without activators were prepared, including 1,4-butanediol (BTD) solution of polyamide (95 %: 5 % by mass ratio), α -terpineol solution of polyamide (95 %: 5 % by mass ratio), α -terpineol solution of ethyl cellulose (95 %: 5 % by mass ratio), and di-propylene glycol methyl ether acetate solution of polyester (95 %: 5 % by mass ratio). These solutions were used to study the functionality of different ingredients, and the choice of solvents was based on the solubility of the ingredients. The polyester, known as Dynacoll 7380, was sourced from Evonik. Other chemicals were obtained from Shanghai Macklin Biochemical Technology Co., Ltd. and used without further purification. The second step involved paste manufacturing, which began with initial manual stirring to pre-blend the components. This was followed by using a high-speed centrifugal mixer operating at 1000 rpm for 3 min to ensure the uniformity of the paste. The pastes were comprised of a 90 % mass ratio of Sn powder (Type 4) powder and a 10 % mass ratio of flux without activators or solvent. The solvent used in this study was primarily to establish a blank benchmark. The solder powder was sourced from the Heraeus Group.

2.2. Preparation of soldered samples

In this study, the normal reflow process was utilized to solder the actual Mini LED onto the substrate, forming a sandwich structure using flux for relevant application studies. Additionally, a formic acid reflow process was introduced to prepare the solder ball for stimulation studies. The use of formic acid in this experiment was to remove activators in the flux system, minimizing the influence of other chemicals and allowing for the study of the self-alignment properties of functional ingredients. For the Mini LED soldered sandwich samples, as depicted in Fig. 3 (a), the preparation process involved stencil printing to deposit the flux onto the PCB substrate using a 35 μm thick stencil with a specific pattern consistent with the PCB substrate. The Mini LED size was 150 μm (length) * 100 μm (width) * 70 μm (thickness), and the pad size was 55 μm * 70 μm * 18 μm , with pre-solder applied to the pad surface through soldering paste, resulting in a thickness of approximately 10 μm . Subsequently, the Mini LED dies from HC SemiTek Corporation were placed on the deposited flux. These LED dies had an Sn/Ag plating layer with a thickness of around 8 μm on the backside. The sandwich structure then underwent the normal reflow process in an N_2 -protected atmosphere (O_2 concentration within 100 ppm) using a reflow oven from Kurtz ersa, following the process as illustrated in Fig. 4. For solder ball samples used for coalescence studies, similar processes were applied, as shown in Fig. 3 (b), involving the printing of activator-free solder paste onto a bare ceramic substrate using a 100 μm thick stencil with a 5 mm circular opening. These samples then underwent formic acid reflow with a series of reflow profiles as depicted in Fig. 5, and detailed reflow conditions are

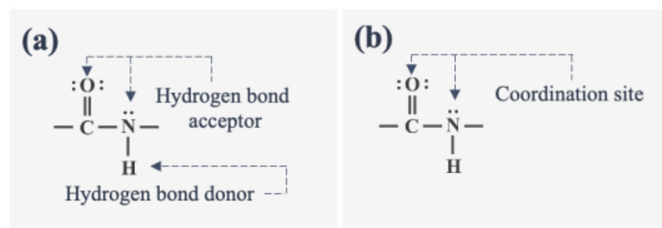


Fig. 1. The chemical structure of the amide group's (a) hydrogen bond donor and acceptor sites, (b) coordination site of ligand.

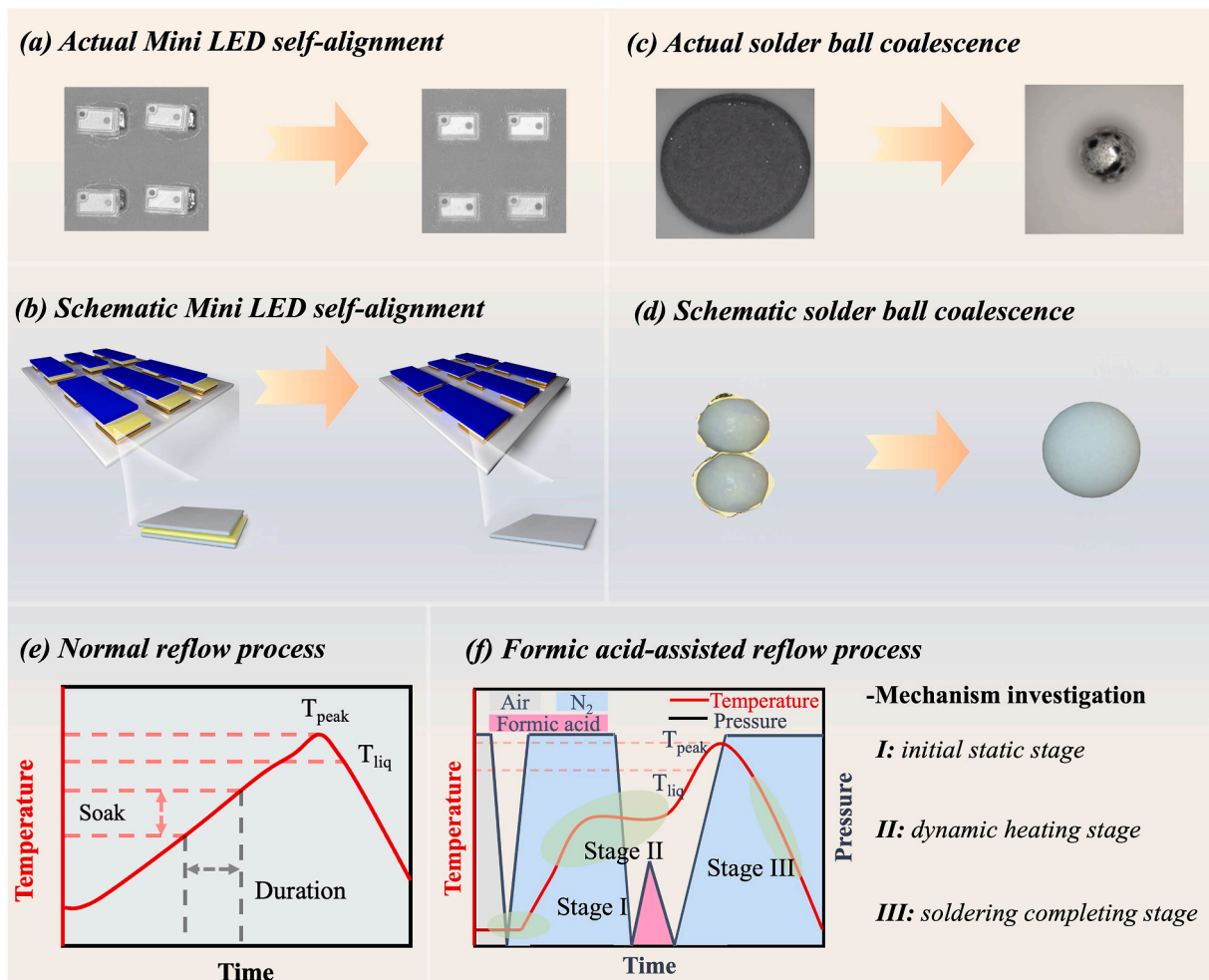


Fig. 2. (a) Actual Mini LED self-alignment, (b) schematic diagram of the Mini LED self-alignment, (c) actual solder ball coalescence, (d) schematic diagram of solder ball coalescence, (e) normal reflow process, (f) formic acid-assisted reflow process.

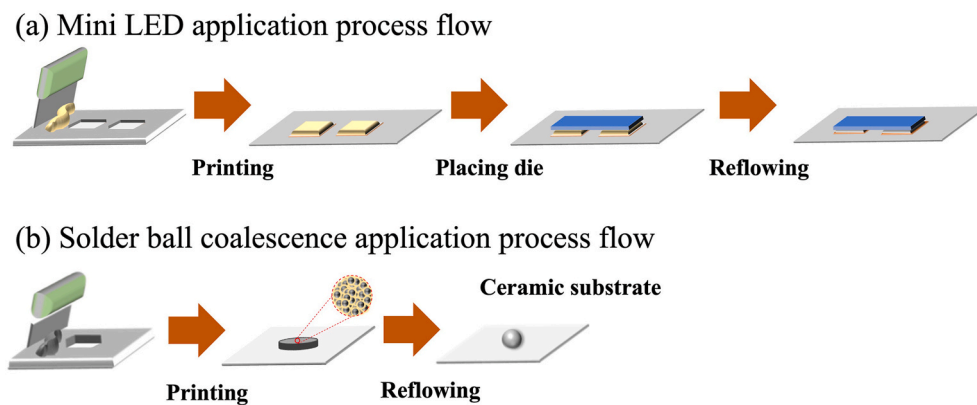


Fig. 3. Schematic diagram of the application process flow (a) Mini LED assembly, (b) solder ball coalescence.

listed in Table 2.

2.3. Inspection of the soldered samples

Following the soldering process, a series of inspections were conducted to investigate the influence of polyamide. For the LED sandwich samples, the self-alignment property was characterized by comparing the lateral distance between the side of the die and the side of the

substrate pad before and after soldering. Furthermore, the shear strength and the void ratio of the solder joint were tested using Nordson DAGE 4000 equipment and Nordson QUADRA5, respectively. Similarly, for the solder ball coalescence sample, the appearance inspection was primarily carried out using the KEYENCE microscope.

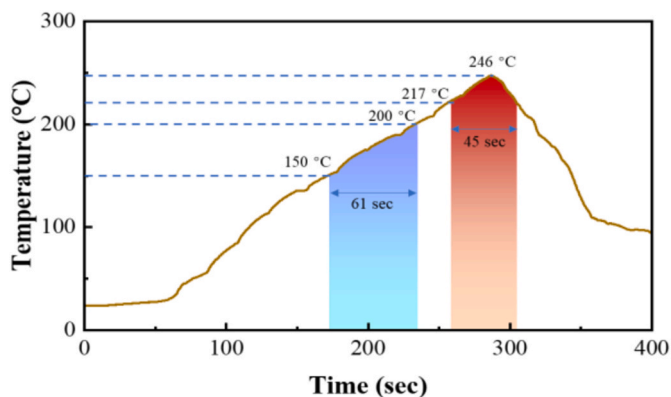


Fig. 4. Schematic diagram of the whole experimental implementation process for solder ball coalescence.

2.4. Characterization methodology

To investigate the fundamental mechanism of self-alignment, solder powder was utilized. The inherent self-alignment property of a tin-based alloy occurs when molten tin aligns itself, and in this study, both the Mini LED dies and substrates were coated with solder, enabling self-alignment between the solder particles. Advanced characterization techniques were employed for the analysis. Fourier Transform Infrared Spectroscopy (FTIR, Thermo Scientific Nicolet iS20) was used to study the changing peak signals of functional groups in polyamide and solvent and to speculate on the interaction among solder powder, polyamide, and solvent. Additionally, Scanning Electron Microscopy with Energy Dispersive X-ray Spectroscopy (SEM/EDS, Japan Electronics Co., Ltd.) was utilized to observe the structure and analyze the element distribution of the interconnections and surfaces among the solder powders following heating treatment but prior to solder melting. The oxidation behavior of the solder powder at elevated temperatures was characterized using X-ray Photoelectron Spectroscopy (XPS, Thermo Fischer,

Formic acid vacuum reflow oven

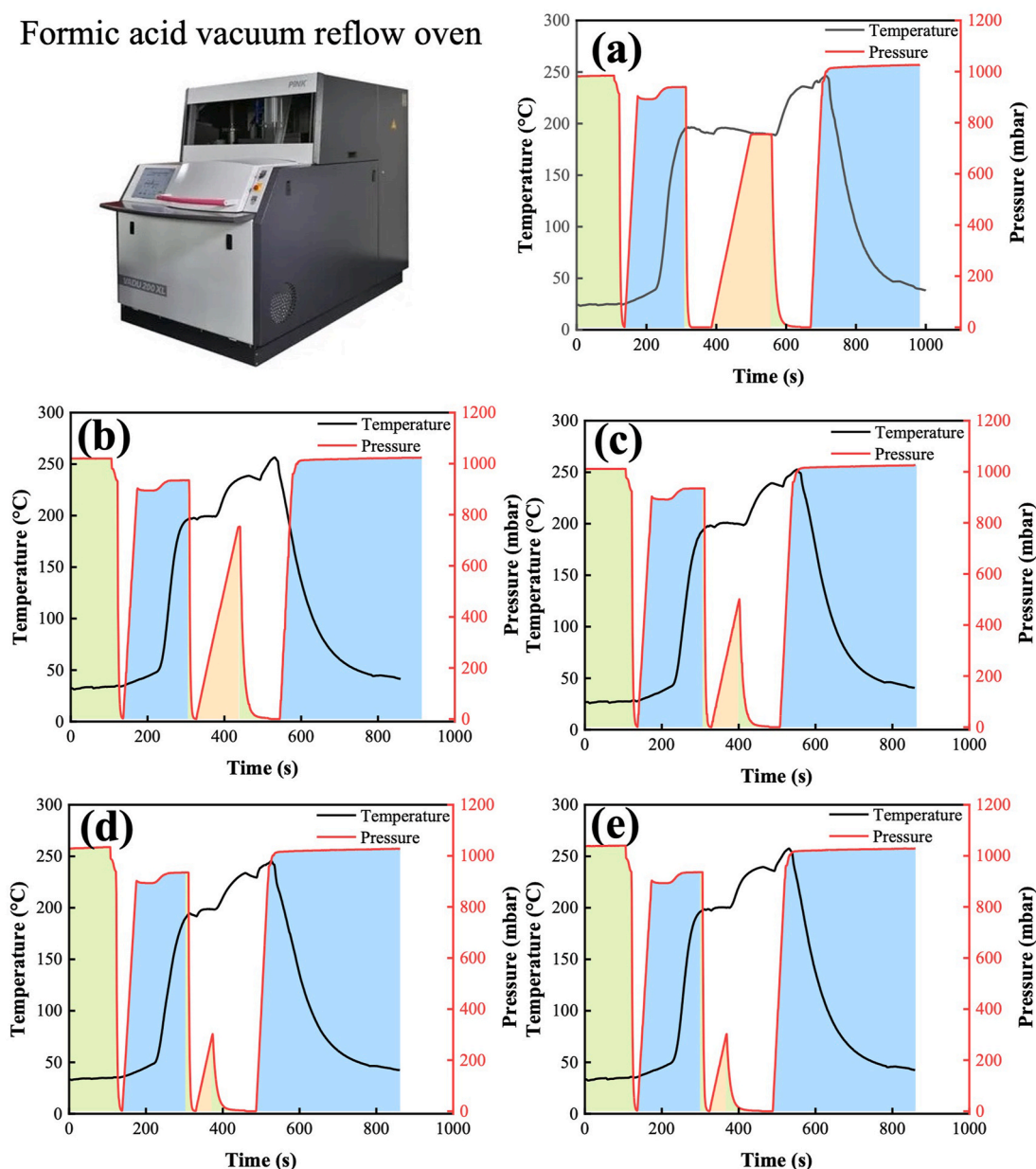
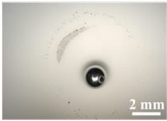
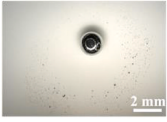
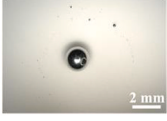
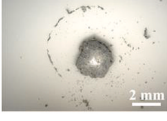


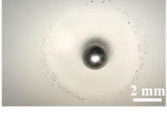
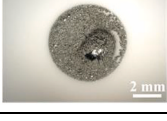


Fig. 5. Various reflow profiles and the equipment used for the formic acid vacuum reflow.

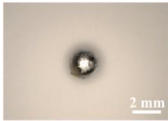
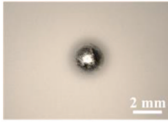
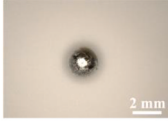
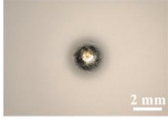
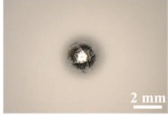
Table 1
Various paste compositions and corresponding solder ball coalescence.

Entry	Paste composition ^a			Solder ball coalescence
	Functional additives	Solvent	Metal	
1	–	α -Terpineol	Solder powder	
2	–	Ester	Solder powder	
3	–	1,4-Butanediol	Solder powder	
4	–	Glycerin	Solder powder	
5	Polyamide	1,4-Butanediol	Solder powder	
6	Polyamide	α -Terpineol	Solder powder	
7	Polyester	Ester	Solder powder	
8	Ethyl cellulose	α -Terpineol	Solder powder	

^a The pastes are composed of 90 w.t%. solder powder, 9.5 w.t%. solvent, and 0.5 w.t%. additives. In another condition, the pastes are composed of 90 w.t%. solder powder, and 10 w.t%. solvent.

ESCALAB Xi+) equipped with an Al K α excitation source ($h\nu = 1486.6$ eV) to study the chemical structure of Sn and O in the oxidized solder powder. Furthermore, Thermogravimetric Analysis-Differential Scanning Calorimetry (TG-DSC) testing was conducted using an SDT-Q600 Synchronous Thermal Analyzer (TA Instrument Company, New Castle, DE) under a nitrogen atmosphere, heated to 400 °C at a ramp rate of 10 °C/min. An Anton Paar rheometer (model: MCR102) was utilized to characterize the viscosity-temperature curve. Measurements were conducted at a constant shear rate of 10 rad/s. The samples were heated at a rate of 1 °C every 15 s, and viscosity was recorded at each 1 °C increment. A total of 126 data points were measured for each flux.

Table 2
The solder ball coalescence among various reflow conditions.

Profile	Temperature			Formic acid		Solder ball coalescence
	PT (°C)	TAL (sec)	ST (sec)	P (kPa)	T (sec)	
a	246.1	130	312	700	170	
b	249.3	136	206	700	110	
c	252.6	141	160	500	70	
d	245.3	135	129	300	45	
e	257.6	160	124	300	45	

PT: peak temperature, TAL: time above liquid, ST: soaking time (150–200 °C), P: pressure.

3. Results and discussion

3.1. PA facilitated the mini LED self-alignment

In this study, we incorporated the functional organic polymer polyamide into commercial soldering fluxes for the assembly of Mini LED components. The evaluation process went through paste printing, die placement, reflow in N₂-protected condition, measuring the lateral distance from the side of the die to the side of the pad before and after reflowing, and inspection, including solder joint shear strength testing and X-ray for calculating the size and distribution of voids.

In both scenarios of using the standard flux and the PA-modified flux, the printed flux on the substrates caused intentional and random displacements of the dies during the LED die bonding process due to the limitations of equipment precision. As shown in Fig. 6 (a), the PA-modified flux demonstrated better self-alignment performance compared to the standard flux, which failed to achieve complete alignment of all the dies to the correct positions. Based on Fig. 6 (c), the distances before reflow between the dies and pad side ranged from 12 μ m to 25 μ m for the standard flux, while the range was from 13 μ m to 28 μ m for the PA-modified flux, as measured according to Fig. 6 (b), the initial standard deviations were 2.8 and 3.0, respectively. After placing the dies onto the substrate, the reflow process was carried out using a normal reflow profile in a nitrogen (N₂)-protected atmosphere with an oxygen (O₂) concentration below 100 ppm. For the standard flux, more than 50 dies out of a total of 80 were properly self-aligned to the desired area with no distance in between, but approximately 25 dies still exhibited noticeable displacement, ranging from 5 μ m to 25 μ m away from the target position. On the other hand, the PA-modified flux achieved nearly perfect alignment, with only a few dies showing slight dis-

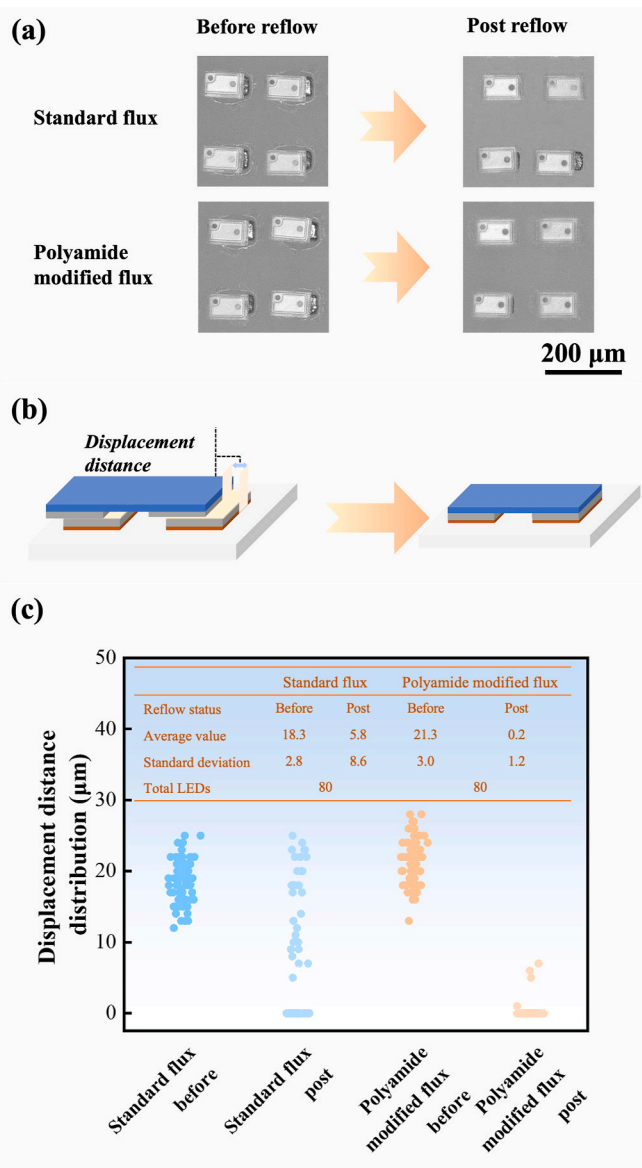


Fig. 6. (a) the actual self-alignment comparison between standard flux and PA-modified flux, (b) the schematic diagram of displacement distance measurement, and (c) the displacement distance distribution before and after reflow for the standard and modified flux.

placements of 1 μm , 5 μm , 6 μm , and 7 μm , respectively. Overall, the average displacement distance for the standard flux before reflow was 18.3 μm , reduced to 5.8 μm after reflow, resulting in a self-aligned distance of 12.5 μm . In contrast, the average displacement distance for the PA-modified flux ranged from 21.3 μm to 0.2 μm , resulting in a self-aligned distance of 21.1 μm . This represents an improvement of 68.8 % compared to the initial intentional displacement distance. Additionally, after reflow, the standard deviation for the displacement distance value increased to 8.6 for the standard flux, while for the PA-modified flux, it decreased to 1.2. This indicates a higher degree of dispersion in the displacement distances for the standard flux post-reflow, suggesting that its self-alignment capability is relatively poorer compared to the polyamide modified flux. The enhanced performance of the PA-modified flux, especially under extreme conditions, demonstrates the potential of organic polymer systems to achieve better alignment during practical soldering processes. Furthermore, process optimization such as refining the reflow profile, adjusting stencil thickness, stencil opening, metallization, and printing parameters may further enhance the self-alignment

capability.

3.2. Solder ball coalescence performance with different functional chemicals

The experimental results reveal a impact of organic materials on solder ball coalescence, as evidenced by the results presented in Table 1, specifically in profile a. When solvents alone, such as α -terpineol, 1,4-butanediol, and di-propylene glycol methyl ether acetate, were used, the solder particles failed to fully coalesce into a single solder ball. Moreover, the use of glycerol as a solvent impeded the wetting of the solder particles, greatly hindering solder ball coalescence. However, when solutions of polyamide in α -terpineol or polyamide in 1,4-butanediol were employed, complete coalescence of all solder particles was achieved. On the other hand, when a solution of polyesters in di-propylene glycol methyl ether acetate was used, the solder particles did not fully coalesce into a single solder ball. Furthermore, the α -terpineol solution with ethyl cellulose as the matrix exhibited no wetting, resulting in the inability to achieve solder ball coalescence. The underlying reasons for these observations are highly complex, as organic materials may impede the activation process of solder by formic acid or hinder the fusion between solder particles, ultimately preventing complete solder ball coalescence or wetting. Future research efforts will primarily focus on investigating the mechanisms through polyamide promotes solder ball coalescence.

3.3. The influence of the process window on solder ball coalescence performance

The in-depth investigation of the adaptability of the 1,4-butanediol solution of polyamide, which demonstrated optimal solder ball coalescence, was conducted under various reflow environments, as depicted in Fig. 5. Various peak temperatures, above liquid time, soaking temperature and duration, the temperature and duration of formic acid were taken into consideration. The summarized findings are presented in Table 2. The phenomenon of solder ball coalescence demonstrated robust characteristics across the aforementioned diverse conditions exhibiting commendable adaptability within the process window.

3.4. Polyamide facilitating tin self-alignment mechanism study

The organic material system exhibits substantial interplay not only during the reflow process but also in the initial state of the activator-free solder paste, establishing a fundamental basis for subsequent reactions. By employing a comprehensive set of characterization techniques, the study encompasses the entire process, from the initial state to the completion of the solder joint. In-depth exploration of the underlying mechanisms was conducted through a series of advanced characterization techniques, including X-ray Photoelectron Spectroscopy (XPS), Scanning Electron Microscopy (SEM), Fourier Transform Infrared Spectroscopy (FTIR), and Differential Scanning Calorimetry (DSC).

The chemicals not only perform their functionality for reflow promotions but also bring benefits for the initial stage. To investigate the mechanism, three main stages were divided along the whole process: I. The initial static stage, II. The dynamic heating stage, III. The soldering completing stage.

3.4.1. Initial static stage

3.4.1.1. FTIR characterization among polyamide, tin powder, and solvent. FTIR was carried out to explore the interaction among solder powder, PA, and BT. The comparison groups consisted of PA-BTD (a solution of 5 % polyamide in BT), Sn PA-BTD 90 % (a activator-free solder paste of the PA-BTD solution with 90 % solder powder), Sn PA-BTD 90 % Drying (the aforementioned solder paste after drying), which are shown in

Fig. 7 (a), (b), (c) and (d), respectively. The drying conditions involved placing the solder paste in an oven at 150 °C for an hour to ensure the complete evaporation of solvents. As depicted in Fig. 7 (a), the main characteristic peaks of polyamide appeared in the spectral analysis, with 3300 cm^{-1} attributed to N–H stretching vibration, 2917 cm^{-1} and 2850 cm^{-1} correlated to C–H stretching vibration, 1631 cm^{-1} referred to C=O stretching vibration, and 1536 cm^{-1} and 1241 cm^{-1} ascribed to N–H bending vibration [37]. Upon blending polyamide with the solvent in small quantities, the main features remained recognizable but showed minor changes. The N–H bending vibration centered around 1242 cm^{-1} found itself obscured; concurrently, a broadened signal developed at 3317 cm^{-1} . This peak broadening arose due to the hydrogen bonding interaction between the hydroxyl group residing in 1,4-butanediol and PA, leading to considerable concealment of the N–H stretching vibration signal. Along with this, the N–H bending vibration exhibited a red shift from 1536 cm^{-1} to 1538 cm^{-1} , and the C=O double bond manifested a red shift to 1636 cm^{-1} . This phenomenon potentially resulted from the electron-attracting tendency of the hydroxy hydrogen bond within the solvent, which brought about a polarization effect on the C=O double bond, leading to a shift toward the red end of the spectrum. The evidence explicitly indicates beneficial cooperation between polyamide and the solvent.

As Fig. 7 (b) shows, with the introduction of pure solder powder to the system, the broadened peak at 3317 cm^{-1} exhibited a red shift to 3328 cm^{-1} . The C=O stretching and N–H bending vibrations displayed slight positional displacements to 1637 cm^{-1} and 1539 cm^{-1} , respectively, suggesting a solid adsorption impact between the system components and the solder powder surface [38,39].

When the majority of solvent evaporated, the main components

remaining in the system are PA and solder powder. As shown in Fig. 7 (c), the peak at 3328 cm^{-1} shifted to 3304 cm^{-1} and changed from a wide peak to a narrow peak, indicating the disappearance of the hydrogen bond system. This may be due to the evaporation of solvents, leading to the disappearance of the majority of the hydrogen bonds. The C=O stretching and N–H bending vibrations exhibited a subtle shift from 1637 cm^{-1} and 1539 cm^{-1} to 1635 cm^{-1} and 1537 cm^{-1} , respectively, suggesting an interaction between PA and the solder powder. Furthermore, Fig. 7 (d) directly compared PA with the dried sample. The N–H stretching vibration red-shifted from 3300 cm^{-1} to 3304 cm^{-1} , the C=O stretching vibration migrated from 1631 cm^{-1} to 1635 cm^{-1} , and the N–H bending vibration moved from 1536 cm^{-1} to 1537 cm^{-1} . A trivial transformation in peak shape appeared at 3304 cm^{-1} , due to broadening caused by hydrogen bonding between polyamide and the oxidation layer on the solder powder surface.

3.4.1.2. SEM characterization of the structure between tin powder and powder. Based on the aforementioned analysis, it is inferred that in the initial state, the variations in signals among different systems suggest the occurrence of specific physical or chemical interactions between PA, the solvent, and the surface of the solder powder. For example, the reactive hydrogen atoms in the N–H group of polyamide may form hydrogen bonds with the oxidized layer on the solder powder surface. Additionally, the oxygen atom in the carbonyl group of polyamide potentially creates hydrogen bonds with the solvent. Moreover, the lone pair of electrons on the oxygen atom participates in the coordination covalent or dative bonding with the vacant orbitals of the metal. After drying the mixture of the PA-butanediol-based system with solder powder, a comparison of SEM characterization was conducted against pure solder

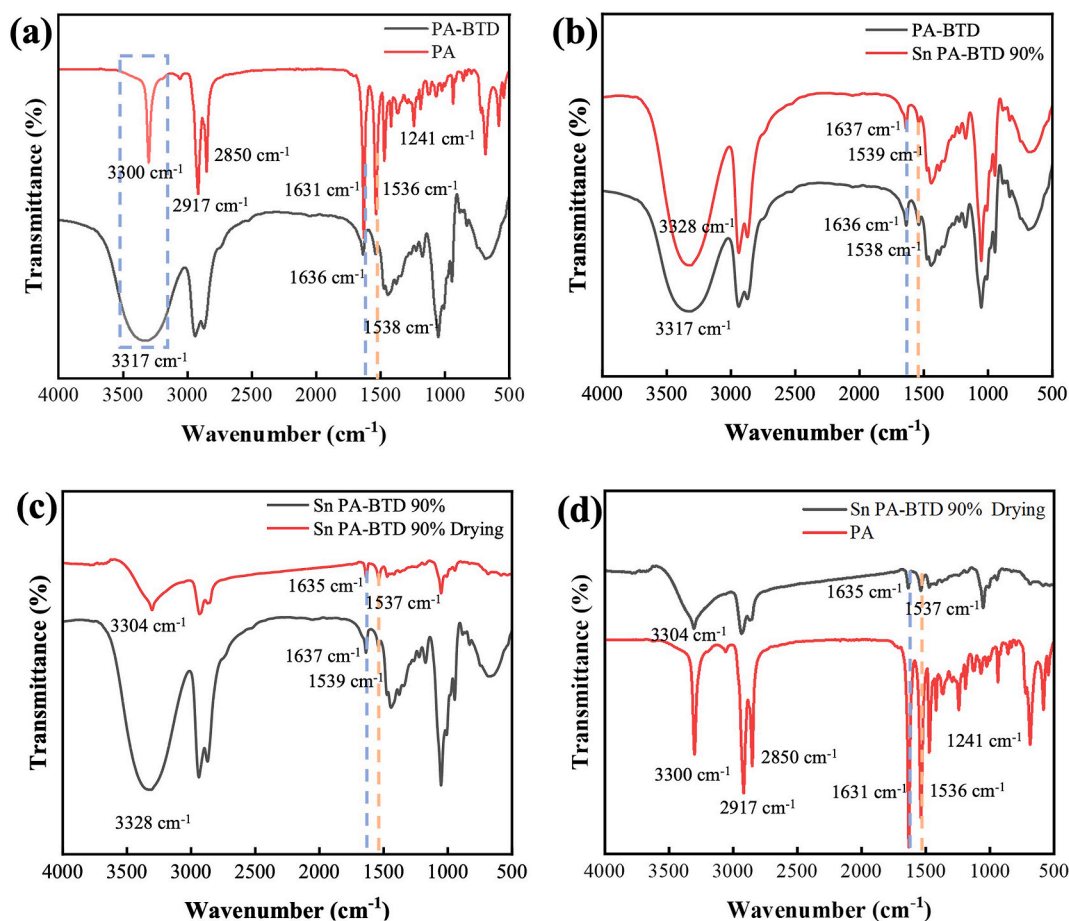


Fig. 7. FTIR spectra comparison of (a) PA-BTD versus PA, (b) PA-BTD versus Sn PA-BTD 90%, (c) Sn PA-BTD 90% versus Sn PA-BTD 90% drying, (d) Sn PA-BTD 90% drying versus PA.

powder. As shown in Fig. 8, unlike the separate existence of pure solder particles, the presence of polyamide generates weak bridges among the solder grains, thus enhancing the adhesion between tin particles. This series of initial state interactions plays a crucial role in establishing interfacial adhesion, forming a solid foundation for the subsequent precise soldering process.

3.4.2. Dynamic heating stage

3.4.2.1. Possible reactions of tin with oxygen and formic acid. During the reflow soldering process, the system is subjected to dynamic thermodynamic changes accompanied by the prevalence of an acidic medium. Tin, serving as a primary metallic constituent, undergoes a multitude of physicochemical transformations during this process, the specific reaction equation is shown in Fig. 9. The series of reactions involved are: (a) The conservative oxidation of solder to form SnO and/or SnO₂ during the heating process, (b) In the presence of formic acid, tin oxide (SnO or SnO₂) undergoes a complex redox reaction, leading to the reduction of solder and the oxidation of formic acid. This process ultimately results in the formation of either Sn²⁺ and/or Sn⁴⁺ ions, respectively, depending on the degree of oxidation initially present in the solder compound. (c) The reaction between elemental solder and formic acid yields the formation of tin ions in either Sn²⁺ or Sn⁴⁺ [40].

This process initiates the generation of a substantial amount of ionized solder that readily diffuses throughout the system. With the presence of vacant orbitals and pronounced polarity, these ionized solder species establish a favorable condition for subsequent interactions to occur. Evident from the reactions mentioned above, it becomes apparent that various chemical states of solder are present throughout the reaction process, encompassing elemental tin (Sn), tin monoxide (SnO), tin dioxide (SnO₂), and the ionic species Sn²⁺ and Sn⁴⁺. Nonetheless, it is important to note that the prevalence and distribution of these forms are influenced by external factors, including temperature and atmospheric conditions prevailing during the reaction.

3.4.2.2. XPS characterization of tin powder oxidation behavior. The surface-sensitive XPS technique was employed to investigate the influence of the reaction process, particularly changes in temperature, on the valence states of tin and the formation of tin salts through the reaction with formic acid. XPS spectral analysis of Sn 3d and O 1s was conducted on the pure solder powder samples before and after heating treatment at 100 °C, as shown in Fig. 10 (a), (b), (d), and (e). Additionally, XPS

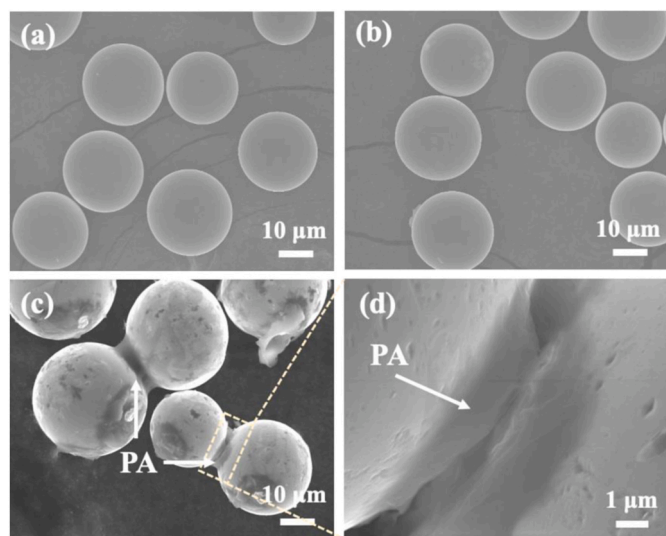


Fig. 8. SEM images of (a) and (b) pure solder powder, (c) PA-treated solder powder, and (d) the neck between solder powder formed by PA.

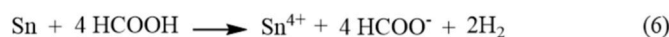
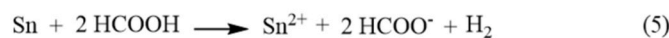
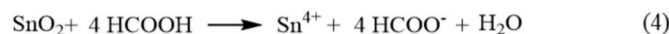


Fig. 9. Various reactions among solder, oxygen, and formic acid during reflow.

analysis was performed on the reaction product of oxidized tin and formic acid as depicted in Fig. 10 (c) and (f).

The Sn 3d_{5/2} and Sn 3d_{3/2} spectra in Fig. 10 (a) and (b) could be deconvoluted into three peaks, corresponding to Sn (IV), Sn (II), and elemental Sn based on their binding energies. For example, in the Sn 3d XPS spectra of unsoldered tin, peaks with binding energies of approximately 486 eV and 495 eV could be assigned to Sn 3d_{5/2} and Sn 3d_{3/2} of Sn (IV), respectively. Peaks with binding energies of approximately 485.9 eV and 494.3 eV could be assigned to Sn 3d_{5/2} and Sn 3d_{3/2} of Sn (II), respectively. Peaks with binding energies of approximately 484.7 eV and 492.9 eV could be assigned to Sn 3d_{5/2} and Sn 3d_{3/2} of elemental Sn, respectively [40].

Upon heating the tin-based solder powder, similar peak signals were observed, with negligible shifts in the binding energy. However, the ratio of the three different Sn valence states changed from an initial ratio of 27.63: 14.36: 58 to 8.46: 29.01: 62.53 after the heat treatment, indicating accelerated oxidation of the solder to form Sn (IV) with increasing temperature. Sn (IV) reacts with formic acid to form Sn⁴⁺. The O 1s signals also exhibited two peaks corresponding to O–Sn (IV) and O–Sn (II), providing further evidence for this assumption.

Furthermore, an experiment was conducted to thoroughly investigate the products resulting from the reaction between solder and formic acid. A solution of formic acid was mixed with solder powder and stirred for 5 min. The supernatant was then separated and subjected to a drying process, followed by XPS analysis of Sn 3d and O 1s, as shown in Fig. 10 (c) and (f). The peaks observed at 486.8 eV and 495.3 eV were attributed to Sn 3d_{5/2} and Sn 3d_{3/2} of Sn (IV), while the peaks at 485.6 eV and 494.7 eV were attributed to Sn 3d_{5/2} and Sn 3d_{3/2} of Sn (II). The ratio of Sn (II) to Sn (IV) was determined to be 96.12: 3.88, which is higher than the initial ratio. Deconvolution of the O 1s peaks also revealed clear signals, indicating the presence of tin oxide and tin dioxides. This could be attributed to the decomposition of tin formate compounds, resulting in the formation of Sn elements and subsequent oxidation to tin oxide. From the ratio analysis, it is inferred that SnO₂ is predominant, which aligns with previous experiments showing the rapid oxidation of tin to SnO₂. Overall, these results indirectly suggest that the primary product of the solder's interaction with formic acid is Sn⁴⁺ ions. This finding paves the way for future investigations into the underlying mechanisms from a theoretical standpoint.

Based on the above characterization methods, it is concluded that the actual process of formic acid reflow soldering induces the generation of tin ions, mainly Sn⁴⁺, leading to the availability of abundant vacant metal orbitals. Concurrently, the amide group in the paste system contributes lone pair electrons. An initial hypothesis proposes the possible coordination reaction between ionic tin and PA, which results in a robust protective layer on the solder powder surface, while also promoting mutual adsorption interparticle adhesion among solder particles and finally, facilitating the coalescence of solder powder to form a solder

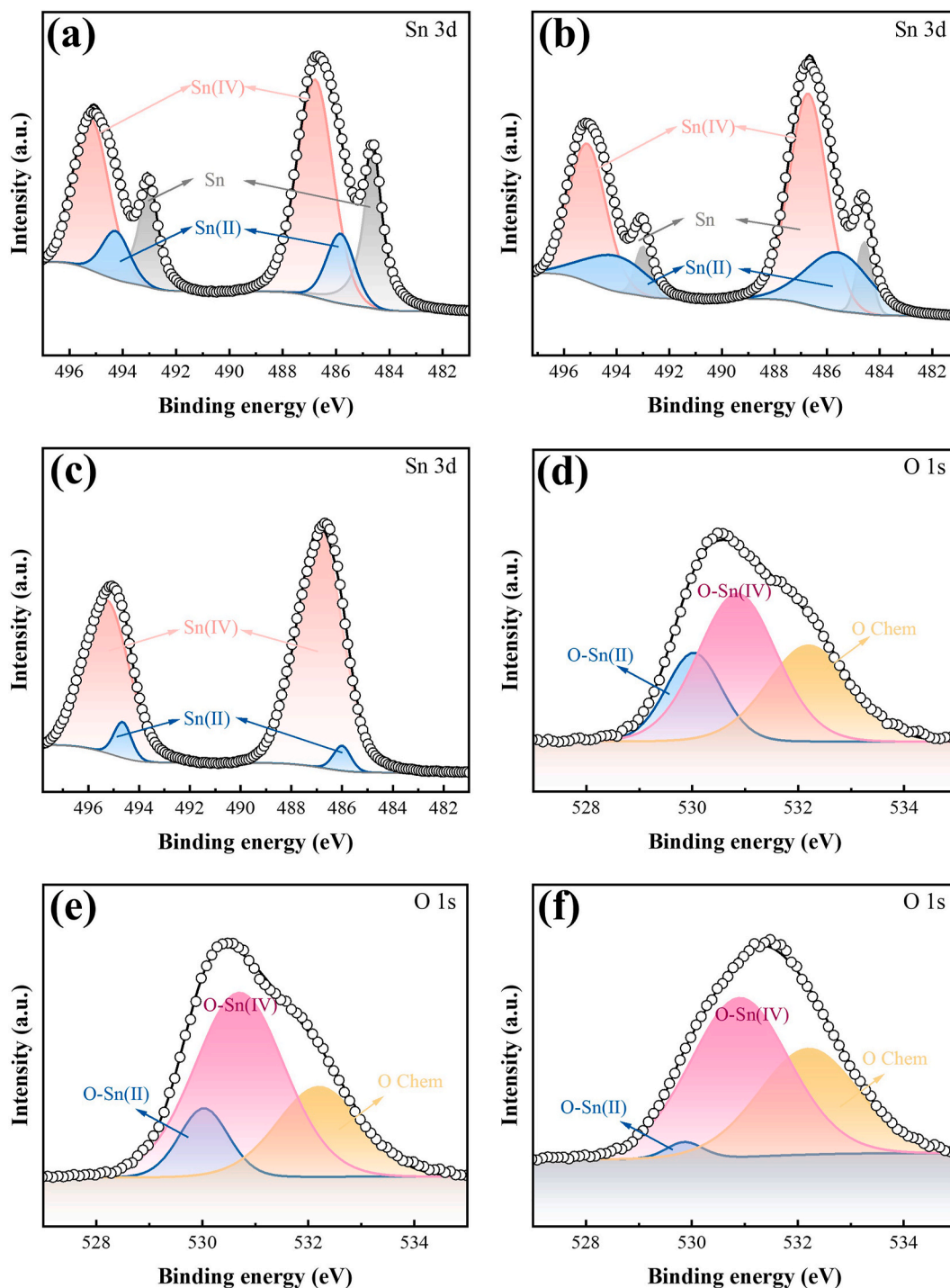


Fig. 10. Sn 3d XPS spectrum of (a) solder powder before heating, (b) solder powder after heating, (c) the reaction intermediate of solder powder and formic acid after drying, O 1s XPS spectrum of (d) solder powder before heating, (e) solder powder after heating, and (f) the reaction intermediate of solder powder and formic acid after drying.

ball.

3.4.2.3. SEM and EDS characterization for the 3D structure. When we directly combined activator-free solder paste with formic acid, we subsequently took a 5 g resultant mixture onto a ceramic substrate and then subjected it to a thermal exposure at 150 °C sustained for an hour. The primary objective of an hour drying step was to evaporate BTD, resulting in a dry powder that facilitates further SEM/EDS characterization. It's worth noting that in a 150 °C environment, formic acid would have

already evaporated well. The outcome of this procedure yielded a solid powder nominated as Sn PA-BTD 90 % FA drying. Interestingly, as shown in Fig. 11(a-c) a 3D interconnected structure was observed nestled between two interspersed solder balls. As magnified, the solder sphere manifested an obvious porous coating. This intriguing emergence of a porous structure brought fascinating advantages. Firstly, it exerted a protective effect by preventing re-oxidation during the temperature increase of the reflow process. Secondly, this intricate three-dimensional framework augments the relative surface area, thereby facilitating an increased exposure of reactive sites and potentially enhancing the

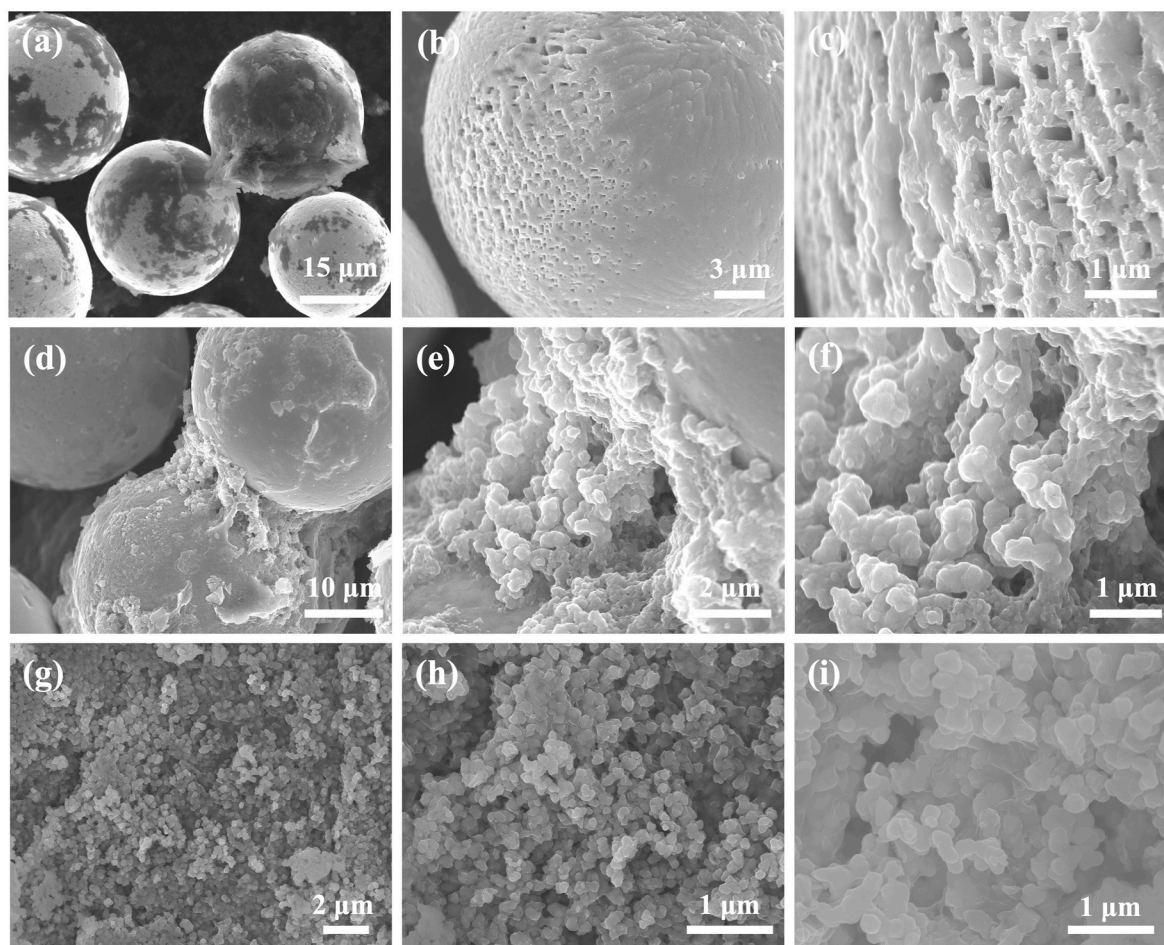


Fig. 11. SEM images of (a) the 3D interconnected structure between solder powders, (b) and (c) the solder powder surface porous coating structure, (d), (e), and (f) the 3D interconnected structure in the neck of solder powders with different magnification, (g), (h), and (i) the 3D structure of PA-CL-FA.

interaction with functional organic ingredients.

Subsequent treatment endowed the solder powder with an orderly three-dimensional surface architecture. Moreover, with this three-dimensional stacking configuration, remarkable bonding was observed at the inter-sphere junctions, enhancing contact and connectivity across spheres. Compared to the initial absorption of pure polyamide at the sphere-sphere junctions, the post-treatment structure displayed improved clarity and amplified conductivity, as discerned in the SEM images of Fig. 11(d–f). This augmented conductivity in the 3-dimensional arrangement implies the presence of conductive substances within the underlying structure. It is reasonable to infer that ionic tin predominantly serves as a potential conductive agent, aligning with previous experimental findings indicating a coordination reaction between ionic tin and polyamide leading to the formation of an interconnected three-dimensional interfacial network. To validate this hypothesis, an experiment performed involved subjecting the supernatant, primarily composed of ionic tin obtained from solder powder and formic acid reactions, to a high-temperature reaction with the 1,4-butanediol solution of PA. The resulting product, upon drying and grinding, appeared as a pale yellow powder nominated as PA-CL-FA. Theoretically, once the solvent is entirely evaporated, the amide functional group contributes an abundance of lone pair electrons. Concurrently, the ionic tin, with its multiple vacant metallic orbitals, facilitates the formation of coordinate bonds, consequently constructing an extensive three-dimensional interfacial network structure. SEM characterization of this yellow powder substantiated the presence of a three-dimensional structure, similar to the initial inter-spherical three-dimensional bonding structure observed, depicted in Fig. 11(g–i).

In addition, it is noteworthy to consider the effect of residual organic matter on the surface of solid tin. Analyzing the composition through energy-dispersive X-ray spectroscopy (EDS) scans, as depicted in Fig. 12, reveals the presence of carbon (C), oxygen (O), nitrogen (N), and tin (Sn) elements. However, the relative contribution of residual organic entities to the overall system is found to be minuscule compared to the dominant solder composition. This empirical evidence strongly supports the premise that the interconnected three-dimensional framework observed among solder spheres is the result of ion-coordinated polymeric assemblies, wherein ionic tin is coordinated with polyamide composition. These findings emphasize the robust intermolecular interactions between organic compositions and solder within the investigated system.

3.4.2.4. FTIR and DSC characterization for the 3D structure. To validate and provide further evidence for these findings, additional characterization techniques were implemented, including energy-dispersive FTIR and DSC.

The FTIR spectrum comparison (Fig. 13 (a)) between the PA-CL-FA system and polyamide reveals notable alterations. The N–H stretching vibration peak experiences a redshift from 3300 cm^{-1} to 3304 cm^{-1} , the C=O bending vibration peak undergoes a redshift from 1631 cm^{-1} to 1634 cm^{-1} , and the N–H bending vibration peak undergoes a red-shift from 1536 cm^{-1} to 1539 cm^{-1} . These changes can be attributed to the involvement of ionic tin, which induces coordination and electrostatic effects that lead to electronic polarization [28,33]. Additionally, upon the introduction of formic acid for an in-situ reaction, various degrees of shift are observed in the N–H stretching vibration, C=O bending vibration, and N–H bending vibration of the solder powder, PA, and 1,

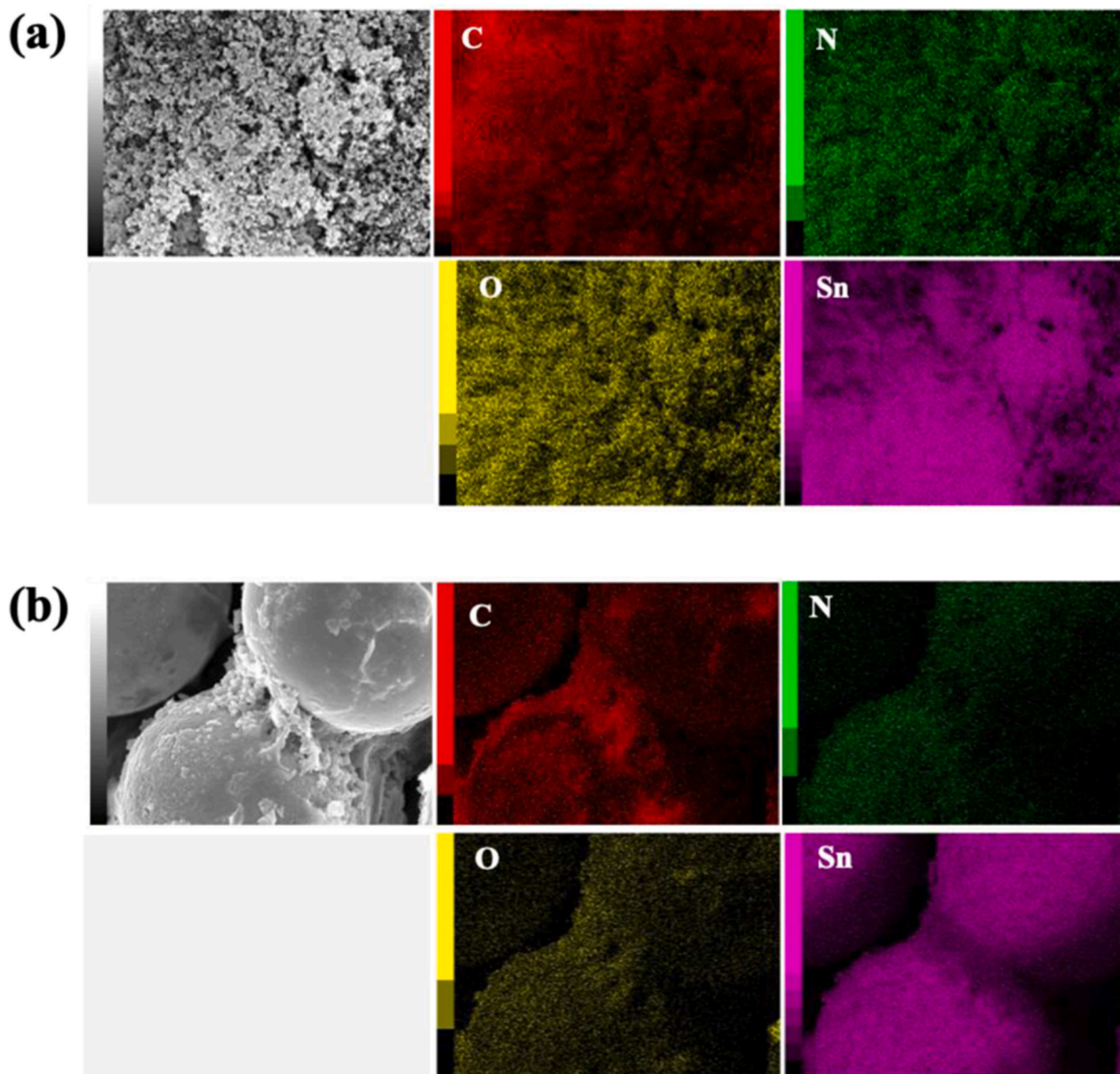


Fig. 12. The EDS mapping of (a) the 3D structure of PA-CL-FA., (b) the 3D interconnected structure in the neck of solder powders with different magnifications.

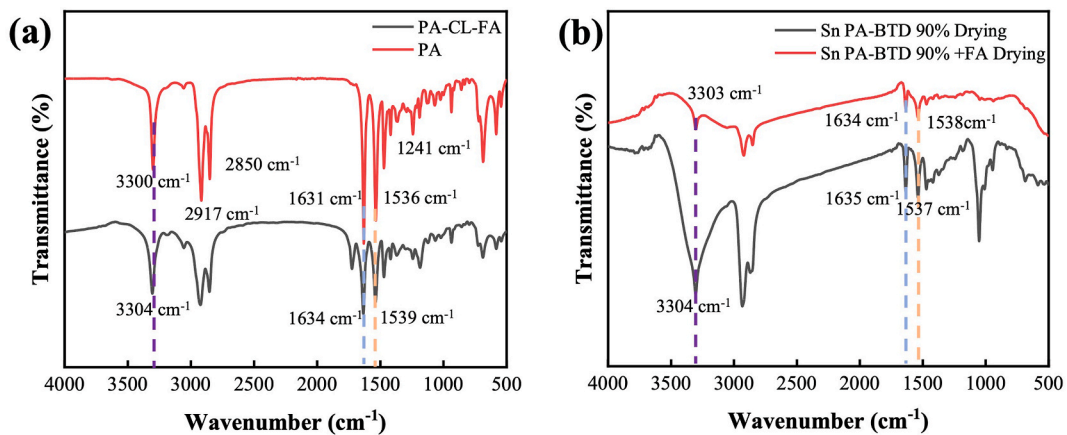


Fig. 13. FTIR spectra comparison of (a) PA-CL-FA versus PA, (b) Sn PA-BTD 90% drying versus Sn PA-BTD 90% +FA drying.

4-butanediol systems, as shown in Fig. 13 (b). This provides indirect evidence of interactions between ionic tin and PA, as indicated by the disruption of the pre-existing hydrogen bond-stabilized system.

The DSC curve (Fig. 14) exhibits multiple overlapping endothermic peaks around 133 °C, 166 °C, and 196 °C for polyamide. These peaks correspond to the softening and breaking of hydrogen bonds, resulting in the absorption of heat. Notably, at approximately 405 °C, an endothermic peak emerges, suggesting polyamide decomposition. However, the introduction of ionic tin into the molecular structure of polyamide leads to the disappearance of the consolidated endothermic peak around 133 °C, 166 °C, and 196 °C, a new peak appears around 220 °C, and the decomposition peak shifts to approximately 428 °C. This demonstrates that ionic tin effectively disrupts the hydrogen bonding network of PA, replacing it with a more stable coordination framework, consequently enhancing the system's stability.

3.4.3. Soldering complete stage

Post soldering process, yielded the solder ball as depicted in Fig. 15 (a), then subjected to cross-sectional analysis, Fig. 15 (b) shows a cross-sectional sample of the solder ball, (c) is the enlarged drawing of (b), Fig. 15. (d) shows SEM images of the sample, there is no obvious organic residual was observed. Further studied the surface through EDS to investigate the presence of organic compounds. The elemental composition of the soldered samples was determined, and the results are summarized in Table 3. The analysis revealed a nitrogen content of 4.71 % and an oxygen content of 19.69 %, whereas no detectable organic carbon was observed. The remaining elemental constituents were primarily metal elements, with solder being the predominant component. The presence of nitrogen in the samples is attributed to the nitrogen-rich atmosphere within the testing chamber during the analysis. Similarly, the majority of the detected oxygen likely originated from the ambient air inside the testing chamber, with a minor contribution from metal oxide species. These findings indicate that any organic compounds present during the soldering process did not substantially accumulate within the metallic matrix of the soldered solder balls. The absence of detectable organic carbon further supports this observation. The observed phenomenon is attributed to the behavior of molten solder under the influence of surface tension during the soldering process. Molten solder tends to expel and exclude any foreign materials or organic residues from the metal system, resulting in a relatively clean and pure metallic structure. Consequently, the soldering process appears to have effectively minimized the retention of organic compounds, leading to a predominantly metal-based composition within the soldered joints.

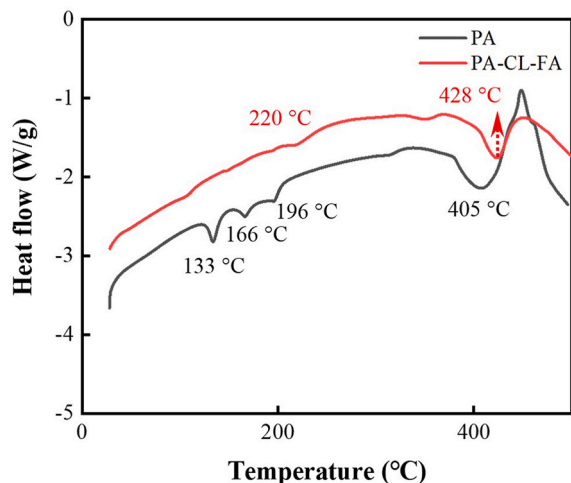


Fig. 14. DSC spectra comparison of PA versus PA-CL-FA.

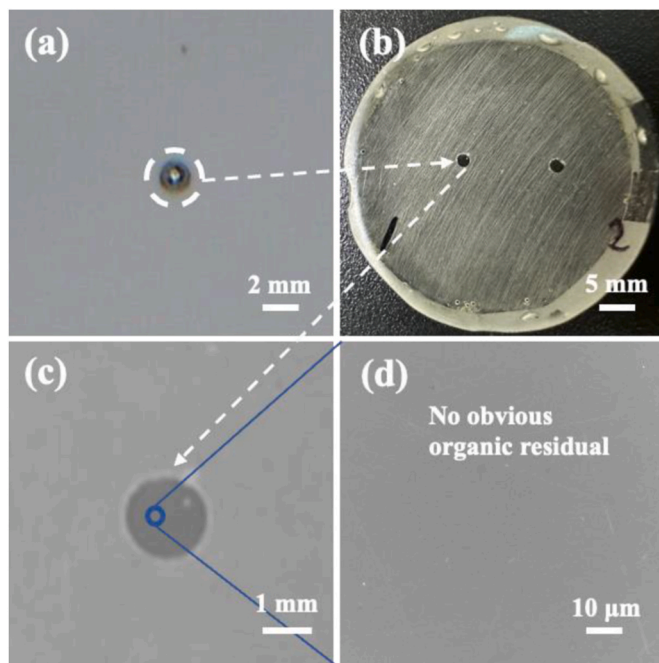


Fig. 15. (a) the actual solder ball formed after soldering, (b) the cross-sectional sample of the solder ball, (c) the enlarged drawing of (b), and (d) the SEM of the cross-sectional microstructure of the solder ball.

Table 3

The elemental composition of the soldered sample.

Entry	Element	Atomic ratio/%
1	N	4.71
2	O	19.69
3	C	ND
4	Sn	71.18
5	Others	~

3.5. Viscosity-temperature curve between two fluxes

Considering that the viscous resistance of the flux may impede the self-alignment brought about by the gathering of tin, mainly driven by the surface tension of molten tin, we utilized an Anton Paar rheometer to conduct tests, measuring the viscosity-temperature curves of standard flux and polyamide modified flux in the range of 25–150 °C. Viscosity was measured at every 1 degree Celsius. The upper-temperature limit of 150 °C was selected because solvent evaporation was observed at that temperature during the actual testing process. As shown in Fig. 16, the viscosities of both standard flux and polyamide-modified flux were found to decrease as the temperature increased. Between room temperature and 80 °C, a notable decrease in viscosity was observed, which slowed and stabilized between 80 °C and 150 °C. This behavior can be attributed to the abundant hydrogen bonds within the flux which are sensitive to temperature changes, leading to their substantial dissociation, particularly in the lower temperature range. Between 40 °C and 80 °C, the viscosity of standard flux was higher than that of the polyamide-modified flux, possibly due to the introduction of polyamide, which increases the density of hydrogen bonds, resulting in a more pronounced viscosity reduction as these bonds break. At 150 °C, the viscosity decreased to 0.02 Pa·s for standard flux and to 0.04 Pa·s for polyamide modified flux. Surprisingly, the polyamide modified flux, known for its superior self-alignment effect, exhibited slightly higher viscosity at high temperatures compared to the standard flux. This leads us to believe that in this system, the viscous resistance of the flux has a minor impact on self-alignment. In combination with preceding studies,

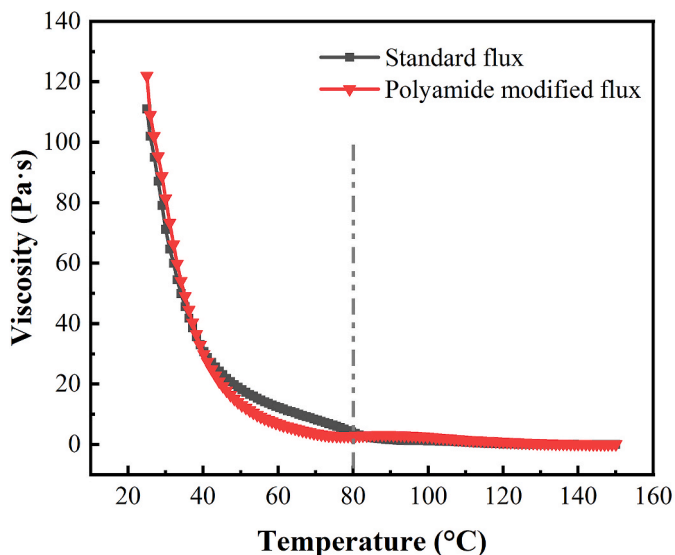


Fig. 16. The viscosity-temperature curve comparison between standard flux and PA-modified flux.

the chemical role of the flux is also a factor affecting self-alignment. In particular, for polyamide, its abundant amide groups provide numerous active sites. In the initial static stage, it serves as an important hydrogen bond donor and acceptor and also acts as a ligand at high temperatures, facilitating its enhancement of self-alignment capability by forming complexes with metals and their ions.

3.6. Soldering performance comparison between two fluxes through Mini LED assembly

Further comparative assessment was conducted, focusing on the void distribution and shear strength as critical parameters indicative of soldering performance. The void distributions in solder joints, as depicted in Fig. 17, share a similar void distribution range for both the standard flux and the PA-modified flux. The standard flux displays a predominantly zero void concentration in most die sites, albeit with certain instances recording a void range from 1.4 % to 7.4 %. Intriguingly, this void distribution parallels the PA-modified flux, with a majority converging to a 0% voiding and a similar range of 1.3 %–7.2 % in select cases. Overall, the average void ratio observed in standard flux is 0.55 %. When contrasted the PA-modified flux, exhibits an average void ratio

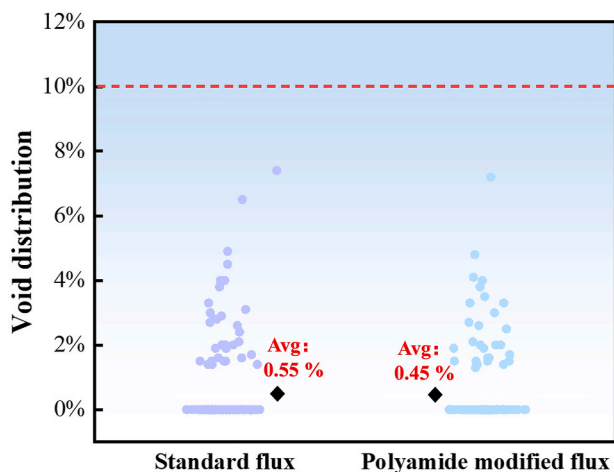


Fig. 17. The void distribution comparison between standard flux and PA-modified flux.

of 0.45 %, and there is no statistically obvious difference observed. Given that the generally acceptable specification for solder voiding is within a 10 % limit, both fluxes adhere to this industry standard.

The shear strength data, represented in a half violin plot in Fig. 18, shows an overall range from approximately 10 g–30 g for both flux types. The shear strength values for the standard flux are observed to range from approximately 7 g–30 g. However, certain data points fall around or below 10 g, possibly attributed to the misalignment leading to insufficient joint contact. Conversely, the data distribution for the PA-modified flux, although displaying a similar range, is noticeably shifted towards a higher shear strength region. This characteristic is bolstered by the clustering of data around the 20 g mark. Irrespectively, a few outliers exist at the 10 g and 12 g levels, attributable to occasional incidences of die misalignment. A comprehensive evaluation of the data sets denotes a superior shear strength performance for the PA-modified flux, corroborating the findings related to die misalignment tendencies. These results represent strides in identifying potential modifications for enhancing micro-soldering performance and provide a basis for future investigations.

The samples soldered with the two flux types were subjected to cross-sectional analysis and examined using SEM, as illustrated in Fig. 19. Fig. 19 (a) and (b) display the SEM cross-sectional images of Mini LEDs soldered with standard flux and PA-modified flux, respectively. Fig. 19 (c) depicts the solder interface when using standard flux, and Fig. 19 (d) shows a similar interface but with PA-modified flux. Further magnification of the solder interfaces to inspect the interaction between the tin and the copper substrate revealed well-defined microstructures at the interfaces with both flux types. Regardless of the use of the standard flux or PA-modified flux, the intermetallic compounds (IMCs) formed maintained a consistent thickness, ranging between 2 and 3 μm . The IMC layer mainly consisted of tin-rich phases, especially Cu_6Sn_5 , which are crucial for the mechanical and electrical integrity of the solder joints. Importantly, these investigative findings elucidate that the incorporation of PA into the flux composition does not compromise the microstructural integrity of the solder joints. On the contrary, this modification appears to facilitate improved joint alignment and robustness.

3.7. Proposed mechanism

Based on the comprehensive characterizations and results presented above, as Fig. 20 describes, we hypothesize the mechanism underlying the construction of a three-dimensional coordination network that

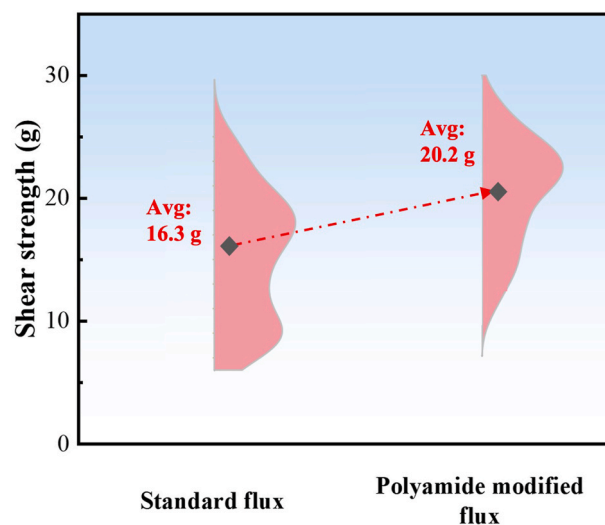


Fig. 18. The shear strength comparison between the standard flux and PA-modified flux.

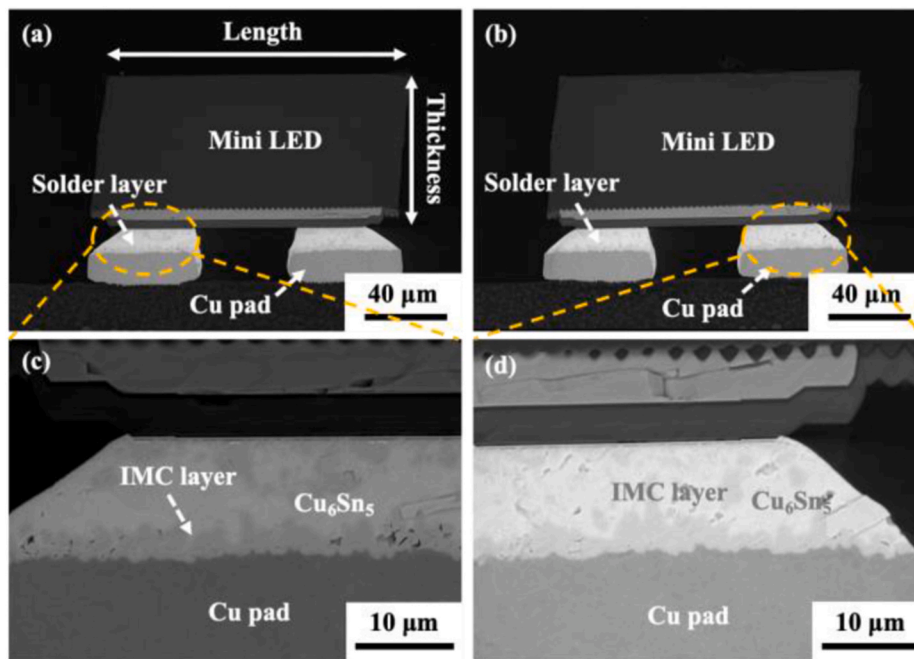


Fig. 19. SEM cross-sectional images of Mini LED solder joint using (a) standard flux, (b) PA-modified flux, detailed SEM images of solder interface using (c) standard flux, and (d) PA-modified flux.

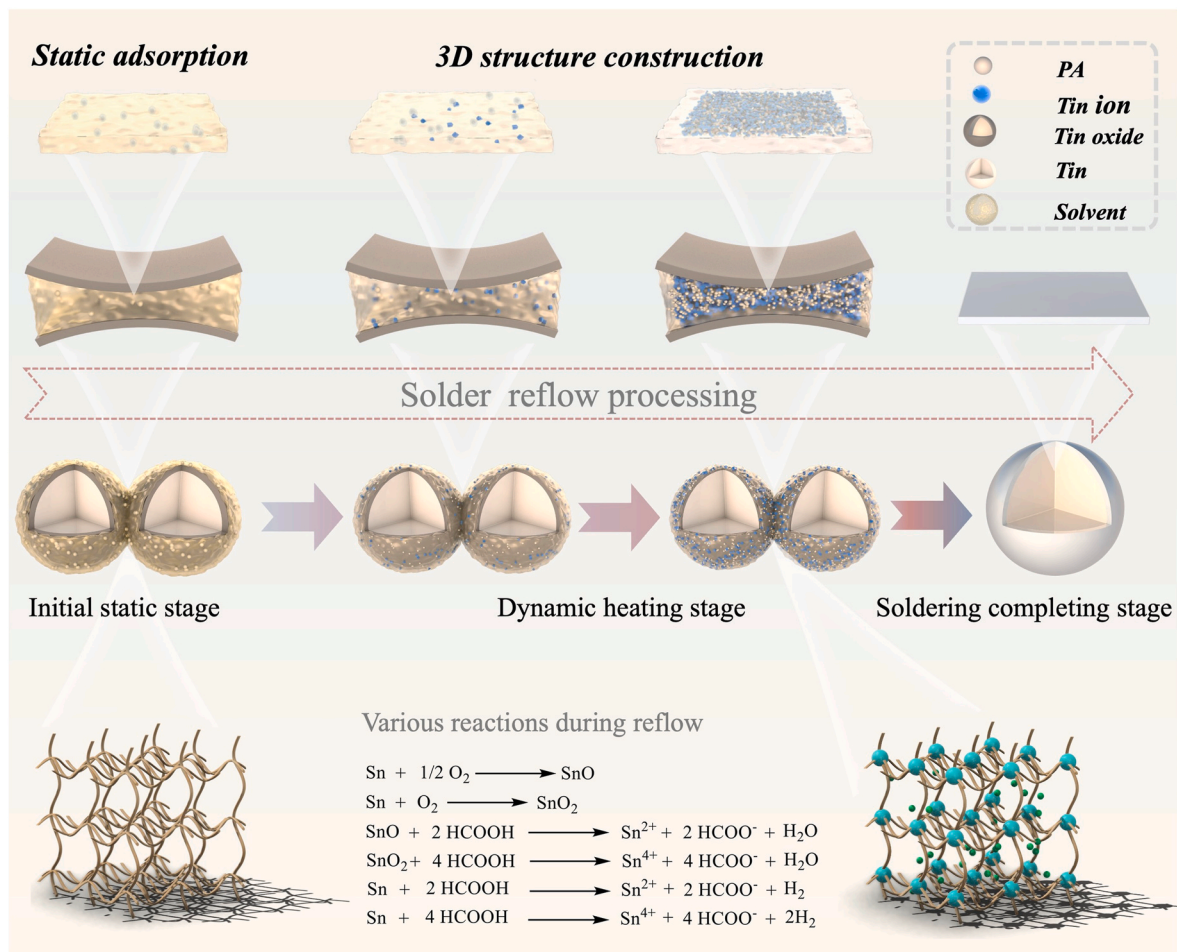


Fig. 20. The schematic diagram of the proposed mechanism.

facilitates precise soldering processes. Initially, the polyamide solution containing 1,4-butanediol fosters an extensive hydrogen bonding system that interacts with the solder surface through hydrogen bonding and electrostatic interactions, leading to robust adsorption. As the reflow process proceeds, formic acid effectively eliminates the oxide layer on the solder surface, leading to the continuous generation of ionic tin species. Under the influence of temperature, ionic tin coordinates extensively with the amide groups of PA, inducing the formation of a highly intricate three-dimensional network structure. Within this elaborate structure, a substantial number of polar functional groups, predominantly composed of amide groups and hydroxyl groups, are embedded. These active groups effectively engage in interactions with the metal surface through hydrogen bonding and other types of bonding, establishing a dense array of interactions at the surface and forming a resilient three-dimensional coordination interfacial network between the two interfaces [41]. This intricate network effectively engenders a robust encapsulation layer on the solder surface, preventing oxidation. Furthermore, during the soldering process, this coordination network actively promotes mutual attraction between the solder particles, ensuring the seamless progression of soldering. Additionally, the surface tension of molten solder during soldering aids in the expulsion of most organic residues, thereby providing the reliability and stability of the soldering process.

It's imperative for forthcoming research to utilize molecular dynamics simulations to enhance our understanding of the complex mechanisms of how the polyamide facilitates the tin's self-alignment capability in Mini LED assembly process. In future work, other polymers such as polyimide, polyurea or the combination of mixed polymers are possible to provide self-alignment effects as functional polymer systems for facilitating soldering. It's essential for upcoming research to also broaden its perspective to address the assembly challenges of Micro LEDs, adapting to the diversity of mass transfer techniques, which range from laser-induced to stamping and self-assembly methodologies. Micro-LEDs face challenges in the mass transfer process, which includes the trade-off between transfer speed and precision. To achieve high transfer speeds, there is often a compromise in precision. Considering the precision challenges these methods face in terms of chip placement, perfecting the soldering process post-transfer will be crucial to correct any alignment deviations that arise. Concurrently, a comprehensive exploration into the solder joint's response to aging, temperature variations, and mechanical forces will shed light on their sustained structural soundness and the consequent implications for the Mini LED display's operational integrity and efficacy. Undertaking such in-depth studies will yield essential knowledge, serving as a cornerstone for the advancement and refined integration of these sophisticated display technologies.

4. Conclusion

This work investigated the synergistic effects of solder and functional organic chemicals on facilitating self-alignment and addressing displacement issues during the transfer process. Polyamide was identified as an optimal chemical of notable effectiveness through extensive experimentation. When applied to Mini LED packaging flux, a substantial improvement in self-alignment capabilities was achieved, improving the self-aligned distance to approximately 68.8 %, from 12.5 μm to 21.1 μm . Comparisons of voiding and shear strength between conventional flux and polyamide-modified flux revealed no variations, indicating the absence of adverse effects on the solder joints due to the introduction of polyamide. Its efficacy was also confirmed via a novel approach to powder coalescence that emulated the self-alignment behavior characteristic of Mini LED assembly. Polyamide was found to enhance the coalescence of solder balls and demonstrated a broad process window for various reflow profiles.

Advanced characterization techniques such as SEM/EDS, FTIR, DSC, and XPS were employed to gain deeper insights into the underlying

mechanisms. SEM/EDS characterization revealed distinct 3D structures at the interface between tin elements, composed primarily of Sn, C, N, and O elements. A comparative experiment involved exposing the supernatant, mainly consisting of ionic tin from solder powder and formic acid reactions to PA, yielding similar 3D structures composed of the same elements. DSC analysis demonstrated a notable shift in the endothermic peak, supporting PA's contribution to the relative stability of the 3D structures. FTIR provided insights into the dynamic interactions between PA, tin powder, and ionic tin across various stages of the reaction, highlighting the formation and stabilization of the structures. XPS clarified the oxidative behavior of tin during reflow and its reaction with acid to form ionic tin, emphasizing the chemical state changes of tin and the impact of chemical environments on the formation of 3D structures. These methods substantiated the proposed mechanism involving the formation of a three-dimensional polyamide-tin ion coordination interfacial network facilitating solder ball coalescence. The insights garnered from this study present a compelling case for integrating solder and functional organic chemicals to boost the self-alignment capability in Mini LED assembly, thereby propelling the industry closer to precision and efficiency in manufacturing processes and potentially facilitating the adoption of advanced display technologies.

CRediT authorship contribution statement

Liangzheng Ji: Writing – original draft, Methodology, Investigation, Formal analysis. **Jing Zhang:** Supervision, Formal analysis. **Guoqi Zhang:** Supervision. **Pan Liu:** Writing – review & editing, Supervision, Formal analysis, Data curation.

Declaration of generative AI and AI-assisted technologies in the writing process

During the preparation of this work the authors used [Chat GPT 4.0] in order to polish the language. After using this tool/service, the authors reviewed and edited the content as needed and take full responsibility for the content of the publication.

Declaration of interest statement

The authors declared no potential conflicts of interest with respect to the research, authorship, and publication of this article.

Acknowledgment

The authors would like to thank the Fudan University and Heraeus cooperation project in this work.

References

- [1] X. Zhou, P. Tian, C.W. Sher, J. Wu, H. Liu, R. Liu, H.C. Guo, Growth, transfer printing and colour conversion techniques towards full-colour micro-LED display, *Prog. Quant. Electron.* 71 (2020) 100263, <https://doi.org/10.1016/j.pquantelec.2020.100263>.
- [2] Y. Huang, E.L. Hsiang, M.Y. Deng, S.T. Wu, Mini-LED, Micro-LED and OLED displays: present status and future perspectives, *Light Sci. Appl.* 9 (2020) 105, <https://doi.org/10.1038/s41377-020-0341-9>.
- [3] P. Ayush, R. Maddaka, M. Zetian, Recent progress on micro-LEDs, *Light Adv. Manuf.* 4 (2023) 19–542, <https://doi.org/10.37188/lam.2023.031>.
- [4] A.R. Anwar, M.T. Sajjad, M.A. Johar, C.A. Hernández-Gutiérrez, M. Usman, S. P. Łepkowski, Recent progress in micro-LED-based display technologies, *Laser Photon. Rev.* 16 (2022) 2100427, <https://doi.org/10.1002/lpor.202100427>.
- [5] T.I. Kim, Y.H. Jung, J. Song, D. Kim, Y. Li, H.S. Kim, J.A. Rogers, Light-emitting diodes: high-efficiency, microscale GaN light-emitting diodes and their thermal properties on unusual substrates, *Small* 8 (2012) 1643–1649, <https://doi.org/10.1002/sml.201290061>.
- [6] Z. Liu, C.H. Lin, B.R. Hyun, C.W. Sher, Z. Lv, B. Luo, J.H. He, Micro-light-emitting diodes with quantum dots in display technology, *Light Sci. Appl.* 9 (2020) 83, <https://doi.org/10.1038/s41377-020-0268-1>.
- [7] S.-H. Mun, C.-M. Kang, J.-H. Min, S.Y. Choi, W.L. Jeong, G.G. Kim, D.S. Lee, Highly efficient full-color inorganic LEDs on a single wafer by using multiple adhesive

- bonding, *Adv. Mater. Interfac.* 8 (2021) 2100300, <https://doi.org/10.1002/admi.202100300>.
- [8] P.J. Parbrook, B. Corbett, J. Han, T.Y. Seong, H. Amano, Micro-light emitting diode: from chips to applications, *Laser Photon. Rev.* 15 (2021) 2000133, <https://doi.org/10.1002/lpor.202000133>.
- [9] T. Wu, C.-W. Sher, L. Yue, C.F. Lee, S. Liang, Y. Lu, Z. Chen, Mini-LED and micro-LED: promising candidates for the next generation display technology, *Appl. Sci.* 8 (2019) 1557, <https://doi.org/10.3390/app8091557>.
- [10] E. Virey, Z. Bouhamri, P. Mukish, 16.1: MiniLEDs and MicroLEDs in today's markets: status and challenges, *SID Symposium Digest of Technical Papers* 50 (2019) 160–163, <https://doi.org/10.1002/sdtp.13422>.
- [11] S.H. Park, T.J. Kim, H.E. Lee, B.S. Ma, M. Song, M.S. Kim, K.J. Lee, Universal selective transfer printing via micro-vacuum force, *Nat. Commun.* 14 (2023) 7744, <https://doi.org/10.1038/s41467-023-43342-8>.
- [12] D. Lee, S. Cho, C. Park, K.R. Park, J. Lee, J. Nam, S. Kwon, Fluidic self-assembly for MicroLED displays by controlled viscosity, *Nature* 619 (2023) 755–760, <https://doi.org/10.1038/s41586-023-06167-5>.
- [13] K.S. Choi, J. Joo, Y.S. Eom, G.M. Choi, K.S. Jang, C. Lee, J.W. Choi, Simultaneous transfer and bonding (SITRAB) process for micro-LEDs using laser-assisted bonding with compression (LABC) process and SITRAB adhesive, in: 2021 IEEE 71st Electronic Components and Technology Conference (ECTC), 2021, pp. 1607–1613, <https://doi.org/10.1109/ECTC32696.2021.00255>.
- [14] Y. Gong, Z. Gong, Laser-based micro/nano-processing techniques for microscale LEDs and full-color displays, *Adv. Mater. Technol.* 8 (2023) 2200949, <https://doi.org/10.1002/admt.202200949>.
- [15] R. Gujrati, A. Srivastava, P. Vuong, V. Ottapilakkal, Y.N. Sama, T.H. Ngo, A. Ougazzaden, Multiple shapes micro-LEDs with defect free sidewalls and simple liftoff and transfer using selective area growth on hexagonal boron nitride template, *Adv. Mater. Technol.* 8 (2023) 2300147, <https://doi.org/10.1002/admt.202300147>.
- [16] O. Haupt, J. Brune, M. Fatahilah, R. Delmdahl, MicroLED's: high precision large scale UV laser lift-off and mass transfer processes, *Laser-based Micro- and Nanoprocessing XVI* 11989 (2022) 140–146, <https://doi.org/10.1117/12.2610137>.
- [17] J. Li, Z. Liu, P-10.1: transfer process of micro-LED using laser, *SID Symposium Digest of Technical Papers* 54 (2023) 787–788, <https://doi.org/10.1002/sdtp.16412>.
- [18] R. Pan, W. Zhang, H. Cheng, J. Yang, Y. Gong, R. Hu, X. Tian, Capillary self-assembly register microspheres to fabricate anisotropic conductive film used for ultra-fine pitch stable electrical interfacing interconnection, *Adv. Mater. Technol.* 8 (2023) 2300514, <https://doi.org/10.1002/admt.202300514>.
- [19] Z. Pan, C. Guo, X. Wang, J. Liu, R. Cao, Y. Gong, Z. Gon, Wafer-scale micro-LEDs transferred onto an adhesive film for planar and flexible displays, *Adv. Mater. Technol.* 5 (2020) 2000549, <https://doi.org/10.1002/admt.202000549>.
- [20] E. Radauscher, R.S. Cok, C.A. Bower, M.A. Meitl, J.O. Thostenson, *Micro-transfer printing with selective component removal*, US11309197B2 (2022).
- [21] B.K. Sharma, B. Jang, J.E. Lee, S.H. Bae, T.W. Kim, H.J. Lee, J.H. Ahn, Load-Controlled roll transfer of oxide transistors for stretchable electronics, *Adv. Funct. Mater.* 23 (2013), <https://doi.org/10.1002/adfm.201202519>, 1977–1977.
- [22] H. Nishikawa, N. Iwata, Formation and growth of intermetallic compound layers at the interface during laser soldering using Sn–Ag Cu solder on a Cu Pad, *J. Mater. Process. Technol.* 215 (2015) 6–11, <https://doi.org/10.1016/j.jmatprotec.2014.08.007>.
- [23] J. Luo, L.H. Qi, S.Y. Zhong, J.M. Zhou, H.J. Li, Printing solder droplets for micro devices packages using pneumatic drop-on-demand (DOD) technique, *J. Mater. Process. Technol.* 212 (2012) 2066–2073, <https://doi.org/10.1016/j.jmatprotec.2012.05.007>.
- [24] M. Yang, S. Yang, H. Ji, Y.H. Ko, C.W. Lee, J. Wu, M. Li, Microstructure evolution, interfacial reaction and mechanical properties of lead-free solder bump prepared by induction heating method, *J. Mater. Process. Technol.* 236 (2016) 84–92, <https://doi.org/10.1016/j.jmatprotec.2016.04.019>.
- [25] S.G. Hashemabad, Z. Gu, T. Ando, Flux-less direct soldering of aluminum by ultrasonic surface activation, *J. Mater. Process. Technol.* 233 (2016) 135–141, <https://doi.org/10.1016/j.jmatprotec.2016.02.015>.
- [26] P. Veselý, D. Bušek, O. Kramera, K. Dušek, Analysis of no-clean flux spatter during the soldering process, *J. Mater. Process. Technol.* 275 (2020) 116289, <https://doi.org/10.1016/j.jmatprotec.2019.116289>.
- [27] S. Griffith, F.N. Siddiqui, G. Schmitz, Effect of surface roughness and droplet size on solder wetting angles, *ACS Appl. Mater. Interfaces* 15 (2023) 24999–25008, <https://doi.org/10.1021/acsami.3c01411>.
- [28] S.J. Griffiths, P. Jantimaponkij, G. Schmitz, Miniaturization, triple-line effects, and reactive wetting of microsolder interfaces, *ACS Appl. Mater. Interfaces* 12 (2020) 8935–8943, <https://doi.org/10.1021/acsami.9b22512>.
- [29] M. Kaltwasser, U. Schmidt, S. Biswas, J. Reiprich, L. Schlag, N.A. Isaac, T. Stauden, H.O. Jacobs, Core-shell transformation-imprinted solder bumps enabling low-temperature fluidic self-assembly and self-alignment of chips and high melting point interconnects, *ACS Appl. Mater. Interfaces* 10 (2018) 40608–40613, <https://doi.org/10.1021/acsami.8b12390>.
- [30] K.H. Kusters, W. Sesselmann, H. Melzner, B. Friesel, A self aligned contact process with improved surface planarization, *Essderc 88: European Solid State Device Research Conference, IEEE*, 1988, <https://doi.org/10.1051/jphyscol:19884104>.
- [31] T. Liukkonen, P. Nummenpää, A. Tuominen, The effect of lead-free solder paste on component placement accuracy and self-alignment during reflow, *Solder. Surf. Mt. Technol.* 16 (2004) 44–47, <https://doi.org/10.1108/09540910410517040>.
- [32] A. M. Najib, M.Z. Abdullah, A.A. Saad, Z. Samsudin, F.C. Ani, Numerical simulation of self-alignment of chip resistor components for different silver content during reflow soldering, *Microelectron. Reliab.* 79 (2017) 69–78, <https://doi.org/10.1016/j.microrel.2017.10.011>.
- [33] K. Pan, J.H. Ha, V.L. Pham, J. Xu, S.B. Park, The effect of solder paste volume on solder joint shape and self-alignment of passive components, in: 2020 IEEE 70th Electronic Components and Technology Conference (ECTC), 2020, pp. 1289–1297, <https://doi.org/10.1016/j.promfg.2020.01.150>.
- [34] H.P. Park, G. Seo, S. Kim, Y.H. Kim, Effects of solder volume and reflow conditions on self-alignment accuracy for fan-out package applications, *J. Electron. Mater.* 47 (2018) 133–141, <https://doi.org/10.1007/s11664-017-5883-0>.
- [35] H. He, S. Fang, J.H. Qin, X. Wu, X.P. Zhang, Influences of organic acids in the soldering flux system on wettability and self-alignment ability of Sn–3.0Ag–0.5Cu solder paste during reflow process, in: 2022 23rd International Conference on Electronic Packaging Technology (ICEPT), 2022, pp. 1–6, <https://doi.org/10.1109/ICEPT56209.2022.9873445>.
- [36] Y. Otoshi, *Flux Composition and Solder Paste*, 2017. JP2017064783A.
- [37] Q. Ding, T. Zhuang, P. Fu, Q. Zhou, L. Luo, Z. Dong, S. Tang, Alpha-terpineol grafted acetylated lentinan as an anti-bacterial adhesion agent, *Carbohydr. Polym.* 277 (2021), <https://doi.org/10.1016/j.carbpol.2021.118825>.
- [38] J. Wang, W. Wang, Z. Ai, M. Li, H. Li, W. Peng, S. Song, Adsorption toward Pb(II) occurring on three-dimensional reticular-structured montmorillonite hydrogel surface, *Appl. Clay Sci.* 210 (2021) 106153, <https://doi.org/10.1016/j.clay.2021.106153>.
- [39] S. Tang, X. Yang, T. Zhang, Y. Qin, C. Cao, H. Shi, Y. Zhao, Adsorption mechanisms of metal ions (Pb, Cd, Cu) onto polyamide 6 microplastics: new insight into environmental risks in comparison with natural media in different water matrices, *Gondwana Res.* 110 (2022) 214–225, <https://doi.org/10.1016/j.gr.2022.06.017>.
- [40] O. Mokhtari, F. Conti, S.K. Bhogaraju, M. Meier, H. Schweigart, U. Tetzlaff, G. Elger, Characterization of tin-oxides and tin-formate crystals obtained from SnAgCu solder alloy under formic acid vapor, *New J. Chem.* 43 (2019) 10227–10231, <https://doi.org/10.1039/C9NJ02135C>.
- [41] Y.M. Zhong, D. Zhou, B.P. Zhang, J.L. Shen, G.F. Zhu, Z.K. Xu, L.S. Wan, Formation of metal-phytic acid surface coatings via oxidation-mediated coordination assembly, *ACS Appl. Polym. Mater.* 4 (2021) 546–555, <https://doi.org/10.1021/acsapm.1c01446>.